Hydroxyapatite for bone related applications derived from sea shell waste by simpleprecipitation method

C. Suresh Kumar, K. Dhanaraj, R.M. Vimalathithan, P. Ilaiyaraja & G. Suresh

Published online: 14 Apr 2020.

Submit your article to this journal ⤤

Article views: 1208

View related articles ⤤

View Crossmark data ⤤

Citing articles: 5 View citing articles ⤤

THE CERAMIC SOCIETY OF JAPAN

THE KOREAN CERAMIC SOCIETY

Taylor & Francis
Taylor & Francis Group

FULL LENGTH ARTICLE

🔓 OPEN ACCESS ✓ Check for updates

Hydroxyapatite for bone related applications derived from sea shell waste by simpleprecipitation method

C. Suresh Kumar [a,b], K. Dhanaraj [c], R.M. Vimalathithan [d], P. Ilaiyaraja [e] and G. Suresh [f]

aResearch and Development Centre, Bharathiar University, Coimbatore, India; bDepartment of Physics, Thiruvalluvar College of Engineering and Technology, Vandavasi, India; cDepartment of Physics, Arunai Engineering College, Tiruvannamalai, India; dDepartment of Physics, Salem Sowdeswari College (Govt. Aided), Salem, India; eChemistry Divisions, School of Advanced Sciences, Vellore Institute of Technology Chennai Campus, VIT University, Chennai, India; fDepartment of Physics, Aarupadai Veedu Institute of Technology, Vinayaka Mission's Research Foundation, Chennai, India

ABSTRACT

The nano-hydroxyapatite (NHAp), NHAp/PEG and NHAp/PVP have been derived from *Clam shell* by precipitation method. The presence of characteristic FTIR peaks and XRD planes indicates the formation of NHAp. Surface morphology of NHAp, NHAp/PEG and NHAp/PVP appeared to be flake, majorly hexagonal and rod clusters like structure, respectively. Sizes of the NHAp are in nanometer scale and size of NHAp/PVP is the lowest. The poor crystalline nature and high carbonate content presence in NHAp/PVP are assessed through crystallinity index, C/P ratio and CHNS analysis. EDX analysis shows the presence of HAp composition in NHAp. The calculated structural parameters expose that the NHAp/PVP shows favorable mechanical property. Good antibacterial activity is observed in NHAp/PVP against two bacteria strains. Hemolysis study also indicates that NHAp/PVP is non-hemolytic. Formation of complete apatite is found when NHAp/PVP immersed in SBF for 14 days. Thus, the NHAp/PVP derived from *Clam shell* may be useful for bone-related applications.

1. Introduction

Bone is the second mainly implanted tissue after blood in the human body system. The biomechanical properties of bone result from its complex structural arrangement of organic (20–30%) (collagen, noncollagenous proteins and lipids), inorganic components (60–70%) and 5% water [1]. Bone inorganic matrix is mainly composed of hydroxyapatite (HAp; $Ca_{10}(PO_4)_6(OH)_2$) with 3% to 8% of carbonate content [2]. Mechanical properties of the bone are characterized by HAp compositions, its crystalline structure, morphology, particle size and orientation. The crystals are nanometer-sized needle like or rod-like shapes (average length – 50 nm, width – 25 nm and thicknesses 2–5 nm) scattered in the organic matrix and composed of OH^-, Ca^{2+} and PO_4^{3-} groups (closely packed in hexagonal arrangement; space group – $P6_3/m$) [3]. Special behavior and bioactivity of biological apatites could vary with HAp dimensions, low crystallinity and presence of carbonate ions in the lattice [3]. Hence, hydroxyapatite has fascinated interest of several researchers from past few decades.

Hydroxyapatite with required carbonate content has much closer compositional similarity to natural bone minerals. It shows a better bioactivity and is biodegradable [4]. It is widely used as coating for metal prosthesis, orthopedic applications, bone graft, drug and antibiotics carrier in bone–implant interface without showing any cytotoxic effect [5]. Generally, CO_3^{2-} ion can reside in OH^- site (A-type) as well as in PO_4^{3-} sites (B-type) in the apatite lattice [6], and in synthetic powders, some fractions of PO_4^{3-} as well as OH^- groups are replaced by CO_3^{2-} (type AB). Biological apatites are principally type B [7].

In general, the process of getting nano-hydroxyapatite (NHAp) from chemical sources is biologically unsafe and complex. However, naturally derived NHAp has some essential properties such as pore structure, bone-cavity breeding and suitable chemical composition [8] for the formation of bone apatite. Therefore, researchers revolve to the more socio-economically engaging alternative targets such as bio-wastes which include shells, fish bones, bovine bones, teeth and bones of pig for preparing valuable NHAp [9]. Especially, in biomaterials research, biogenic calcium carbonates derived from exoskeletons of arthropods, egg shells, mollusc shells, corals and nacre are attracted a special interest during the last decades [10]. Specifically, bivalves (clamshell) belong to Mollusca (second largest phylum among the invertebrates; 80,000 species). The annual harvest of bivalves for human consumption represents about 5% by weight of the total world harvest. In India, clam

CONTACT G. Suresh ✉ gsureshphy_1983@yahoo.co.in; suresh.physics@avit.ac.in 📄 Department of Physics, Aarupadai Veedu Institute of Technology, Vinayaka Mission's Research Foundation, Chennai, Tamilnadu 603 104, India

production is about 57,000 tones (73.8%) annually. Hence, the conversion of clamshells into NHAp can be beneficial since they are cheap and abundant in nature [11–13].

Over the past decades, a number of synthetic routes had been adopted which include hydrothermal, sol-gel, precipitation, mechano-chemical, mechanical activation and other methods for producing HAp from biowastes. However, some limitations of these methods are expensive precursors, complicated procedures, severe aggregation of the particle and restricted yield. Chemical precipitation method is most promising method to synthesize NHAp and it has more practical advantages which include simple experimental stages, high yield and purity, low energy consumption, low temperature synthesis, homogenous mixing, microstructure property, porous size control, nanophase particle size control, large-scale production and meager amount of harmless by-products [4,14,15].

Unfortunately, low toughness and weak bending strength are the main drawbacks of its uses in load-bearing sites applications [16]. To overcome these mechanical limitations, NHAps were synthesized by adding polymers [16]. Polymer addition during the synthesis is modifying the exterior of nanoparticles and therefore improving the stability and mechanical properties of the materials. Though numbers of polymers are available, polymers like polyvinyl pyrrolidone (PVP) and polyethylene glycol (PEG) (polar polymers) are water-soluble polymers which are used as a capping agent to control the nucleation growth of HAp crystal [17,18].

The present study has intended to extract the NHAp from clamshells via chemical precipitation method. The polymers such as PVP and PEG are used to control the nucleation growth of NHAp to get required mechanical properties and carbonate content. The compounds such as NHAp, NHAp/PEG (synthesized using PEG), NHAp/PVP (synthesized using PVP) were characterized by Fourier transform infrared, XRD, SEM-EDX, carbon-hydrogen-nitrogen-sulfur (CHNS) elemental analyzer, TEM-SAED (selected area electron diffraction), antibacterial, hemolytic activity and SBF analysis. Mechanical property, crystalline nature and amount of carbonate contents (CO_3^{2-}) are assessed using FTIR and XRD analyses. A suitable mechanism is proposed for crystallite size change, morphology variations, CO_3^{2-} substitution, crystalline nature variation and SBF interaction. Successful synthesis of the material shows reserve properties such as enough carbonate content, suitable mechanical properties, apatite forming ability and favorable antibacterial activity and will find many bone-related applications. To the best of our knowledge, this is the first report for the synthesis of NHAp from clamshells using PVP and PEG polymer by chemical precipitation method.
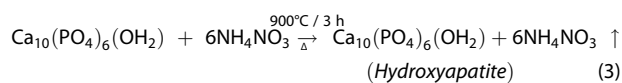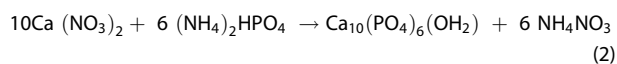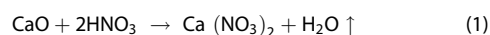
2. Materials and methods

2.1. Materials

The biowaste clamshells (species: *Venerupis philippinarum*) were collected from different sites of Vellar Estuary situated at Parangipet (Lat: 11º20′ 25.55″N, Long: 79º45′ 38.62″E), Tamilnadu, South India. Other importance of the sampling site was reported in our previous article [19]. The shells were thoroughly cleaned with running water several times and soaked in hot water for 30 min to remove meat and algae. The shells were further washed with distilled water and dried at 100ºC in hot air oven for 3 h. Diammonium hydrogen phosphate (($NH_4)_2$ HPO_4), nitric acid (HNO_3), acetone, sodium hydroxide (NaOH), polyethylene glycol (PEG, Mw: 6000), polyvinyl pyrrolidone (PVP, Mw: 40,000) and deionized water were purchased from Merck. All the chemicals were analytical reagent grades and used as such without any purification.

2.2. Synthesis of hydroxyapatite (NHAp)

CaO phase was achieved from the dried shells as per the procedure reported by Dhanaraj and Suresh [19] which was used for preparing NHAp by the precipitation method. It was dissolved in concentrated HNO_3 (25% of nitric acid) completely and then diluted with deionized water to get 0.1 M of $Ca(NO_3)_2$ solution. To this solution, 0.06 M of $(NH_4)_2HPO_4$ solution was slowly added; finally, the obtained amount of Ca/P ratio was 1.67. The pH of the above reaction mixture was adjusted to 9 by adding 1 M NaOH solution. The obtained bright milky precipitate was centrifuged for 15 h and filtered through Whatmann40 filter paper. It was washed several times with deionized water to remove possible residuals such as NaOH and NH_4NO_3. Finally, it was dried at 100°C for 3 h in a hot air oven to obtain NHAp followed by calcination at 900°C for 3 h to obtain crystalline NHAp. The related chemical reactions are given as follows:

$$CaO + 2HNO_3 \rightarrow Ca(NO_3)_2 + H_2O \uparrow \tag{1}$$

$$10Ca(NO_3)_2 + 6(NH_4)_2HPO_4 \rightarrow Ca_{10}(PO_4)_6(OH_2) + 6NH_4NO_3 \tag{2}$$

$$Ca_{10}(PO_4)_6(OH_2) + 6NH_4NO_3 \underset{\Delta}{\overset{900°C / 3 h}{\rightleftharpoons}} Ca_{10}(PO_4)_6(OH_2) + 6NH_4NO_3 \uparrow$$
$$(Hydroxyapatite) \tag{3}$$

2.3. Synthesis of NHAp/PEG and NHAp/PVP

A total of 1 mM of PEG was separately prepared in 25 mL of deionized water. Prepared PEG solution was

added drop by drop to the pure NHAp while the mixture is continuously stirred. The precipitate was washed, dried and calcined to get NHAp and the product is named as NHAp/PEG. For the preparation of NHAp/PVP, the same procedure was followed. Characterization techniques such as FTIR (Perkin Elmer Spectrum One, USA), XRD (X'PERT PRO, Netherlands), SEM–EDX (JEOL-6610, Japan), CHNS (Perkin Elmer series – II 2400 Elemental Analyzer, USA), TEM-SAED (JEOL/JEM 2100, Japan), antibacterial activity, hemolytic activity and SBF analysis were used for analyzing the synthesized samples.

2.4. Antibacterial activity test

The in vitro antibacterial activity of the calcined NHAp, NHAp/PEG and NHAp/PVP samples has been studied against *Escherichia coli* and *Staphylococcus aureus* by the agar well diffusion method as reported in Dhanaraj and Suresh [19]. Using micropipette and plates, negative control and present samples (NHAp, NHAp/PEG and NHAp/PVP) were loaded on marked wells and incubated at 37°C for 24 h. With the help of HiAntibiotic Zonescale in Himedia, the zone of growth inhibition was measured (in mm). All experiments were executed in triplicate under aseptic conditions.

2.5. Hemolysis assay

Hemolysis assay was performed as per the procedure given in Tank et al. [20]. Briefly, 0.8 mL of NHAp/PVP

(1 mg mL^{-1} in phosphate buffer saline (PBS) solution) was added to 0.2 mL of red blood cell (RBC) suspensions. Thereafter, sample was incubated at room temperature for 2 h and shaken to resuspend the RBCs and NHAp/PVP every 30 min. The absorbance of the supernatant was measured by Optical Density (OD) at 560 nm after the sample is centrifuged at 3000 rpm. The hemolysis ratio (H) was calculated by the following formula:

$$H = \frac{A_s - A_n}{A_p - A_n} 100\%$$

Where, H is hemolysis ratio, A_s, A_n and A_p are average absorbance of sample, negative control (1X PBS) and positive control (Deionized water) respectively.

2.6. SBF analysis

The bioactivity of the prepared samples was studied using simulated body fluid (SBF). The solution was prepared by dissolving appropriate quantities of chemicals in distilled water and reagents were added one by one in 1000 ml of water as per the procedure given by Tank et al. [20].

3. Results and discussion

3.1. FTIR spectroscopic analysis

The FTIR spectra of the raw *Clam* shell, NHAp, NHAp/PEG and NHAp/PVP calcined at 900°C are shown in Figure 1(a–d) respectively. Figure 1(a) shows an intense
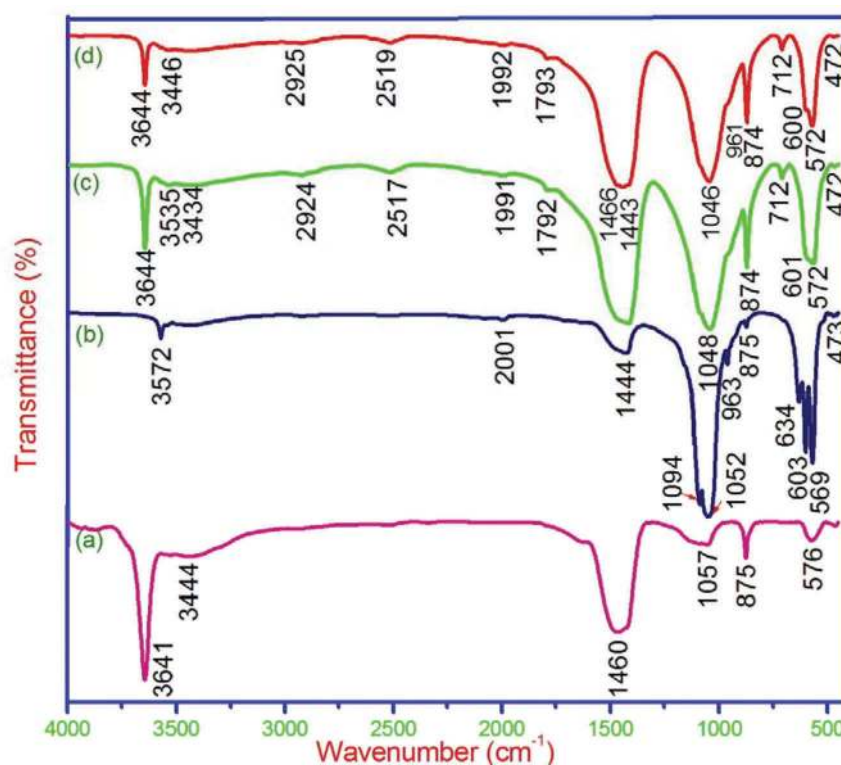

Figure 1. FTIR spectra of the raw *Clam* shell (a), NHAp (b), NHAp/PEG (c) and NHAp/PVP (d) calcined at 900°C.

sharp peak appeared at 3641 cm^{-1} due to the OH$^-$ stretching and characteristic peaks of calcite are observed with less intensity. Formation of CaO at 900°C is assessed by the small characteristic peak at 576 cm^{-1}. Other small changes in the spectra are clearly explained in our earlier study [19]. The same observation was reported in the literature [19,21,22].

According to Youness et al. [23], chemical groups in the FTIR were PO$_4^{3-}$, OH$^-$, CO$_3^{2-}$ as well as HPO$_4^{2-}$ to characterize the NHAp. PO$_4^{3-}$group had four characteristic peaks appear in broad spectrum that represents vibration modes, namely v_1 (weak peak at 963 cm^{-1}; stretching vibration of the O-P-O bond), v_2 (weak band at 473 cm^{-1}; asymmetric stretching vibration of PO$_4$), v_3 (sharp and strong ill-defined peaks at 1052 and 1094 cm^{-1}) and v_4 (double sharp strong peaks at 603 and 569 cm^{-1}; triply degenerated bending mode of the O-P-O) [23]. The peak at 2001 cm^{-1} was assigned to PO$_4$ (v_3, v_1) [10]. The above mentioned characteristic vibration modes are clearly presented in Figure 1(b) and thus prepared sample is HAp. The presence of medium peaks at 634 (libration mode) and 3572 cm^{-1} (stretching vibration) is due to the hydroxyl (OH$^-$) group [24]. According to Nunez et al. [25], CO$_3^{2-}$ bands observed between 1365–1565 cm^{-1} (v_3, asymmetric stretching) and 875 cm^{-1} (v_2, out of plane bend) were accounted for the presence of carbonate content in HAp. In the present case, same observation is made (Figure 1(b)) and thus carbonate content is presented in the NHAp.

Interestingly, when adding the polymers (PEG and PVP) with NHAp (Figure 1(c,d)), intensities of CO$_3^{2-}$ peaks are high. While adding the PEG (Figure 1(c)), the above mentioned characteristic vibration modes of phosphate (v_1, v_2, v_3 and v_4) are observed with slight deviations. Intensity and broadness of the v_4 (603 and 569 cm^{-1}) are decreased and v_3 doublet is changed into singlet at 1046 cm^{-1}. Weak peaks at 634 and 3572 cm^{-1} are disappeared. New minor sharp peak at 712 cm^{-1} and small minor peaks are observed at 1792 and 1991 cm^{-1} (presence of amides), 2517, 2924, 3434 and 3535 cm^{-1} (due to the adsorbed water). As stated by Bang et al. [7], sintering of carbonated HAp at high temperatures (≥900°C) produces HAp and CaO. In the CO$_2$-rich atmosphere, meager amount of CaCO$_3$ is obtained due to the reaction of CaO and CO$_2$. It is expected that mixture of carbonated HAp and CaCO$_3$

is observed after heat-treatment in CO$_2$ atmosphere. The formation of CaCO$_3$ is assessed by the presence of a small peak at 712 cm^{-1}. Some literature [7,26] had reported the same information about this peak. The sharp intense peak at 3644 cm^{-1} suggests the presence of Ca(OH)$_2$ [27].

Fascinatingly, sharp peak at 874 cm^{-1} and doublet at 1443 and 1466 cm^{-1} are strongly registered. Generally, type B carbonate was characterized by 1465, 1412 and 875 cm^{-1} [28,29]. Even some deviations in v_3 carbonate bands, the band at 874 cm^{-1} assigned to bending (v_2) mode undoubtedly confirms carbonate substituted for PO$_4^{3-}$ group (B-type substitution) [27]. In the present study, the presence of B-type carbonate is assessed in NHAp/PEG. Similar observations were reported in the following literature [16,23,27–29]. Decreases in the intensities of the phosphate bands at 963 and 1094 cm^{-1} in NHAp/PEG could be due to the substitution of CO$_3^{2-}$ in PO$_4^{3-}$ [29] and thus carbonate content is increased.

Figure 1(d) shows the FTIR spectrum of NHAp/PVP. Here also all the characteristic vibrational modes of phosphate, carbonate and hydroxyl bands are observed with slight deviations. When compared with Figure 1(c), intensity of v_4 doublet (600 and 572 cm^{-1}) is decreased, whereas the carbonate and Ca(OH)$_2$ peak intensities are increased. The presence of well-defined strong doublet (v_3; asymmetric stretching) at 1443 and 1466 cm^{-1} indicates the strong presence of carbonate in NHAp. These changes also confirm the increased carbonate content in NHAp/PVP. Since nanoparticles can form strong coordination with N–C = O groups of PVP, it would lead to strong adherence of PVP on the surface of particle than PEG and thus high carbonate content is observed in NHAp/PVP [30,31]. FTIR analysis reveals the increasing order of carbonate contents in the NHAp<NHAp/PEG<NHAp/PVP. These observations are further confirmed by calculating carbonate to phosphate ratio (Table 1).

According to Youness et al. [23], the presence of sharp and splitting peaks at 565/605 and 1055/1100 cm^{-1} indicates the high degree of crystallinity. In the present case, the above mentioned splitting peaks are clearly visible, the intensity of splitting is decreased and still decreases (Figure 1(b–d)) in NHAp, NHAp/PEG and NHAp/PVP, respectively. This dictates that NHAp has a high degree of crystallinity, it is

Table 1. Structural parameters, crystallinity index and C/P ratio of NHAp, NHAp/PEG and NHAp/PVP.

Sample ID	Lattice parameters			Volume of Unit cell V (A°)	Average crystalline size D (nm)	Average microstrain (ε) x 10^{-3}	Average Dislocation density (δ) x 10^{14}	Average Stacking fault (SF) x 10^{-2}	CI (FTIR)	CI ((XRD)	C/P
	a = b (A°)	c (A°)	c/a								
NHAp	9.4618	6.8204	0.7201	528.79	51.86	0.5363	3.7182	0.1740	2.8909	1.8040	0.395
NHAp/PEG	9.4481	6.8340	0.7233	528.30	48.14	1.7031`	4.3150	0.5102	2.2654	1.7874	0.411
NHAp/PVP	9.3931	6.8939	0.7339	526.74	32.12	2.0151	9.6927	0.6128	2.2269	1.4640	0.456

decreased for NHAp/PEG and further decreases for NHAp/PVP. These observations are confirmed in the crystallinity index calculations (Table 1).

3.2. Calculation of crystallinity index and carbonate to phosphate ratio

FTIR helps to understand bone quality and fracture risk in osteoporotic patients by calculating parameters related to bone quality such as crystallinity index and carbonate to phosphate ratios. Variation in carbonate-to-phosphate and crystallinity leads to make fracture [2].

3.2.1. Crystallinity index (CI)

The crystallinity index (CI) is a measure of the perfection and degree of ordering in a sample. It correlates linearly with NHAp crystal size and perfection in the c-axis direction, and has obvious influences on hardness and density of the material [2,32,33]. CI is calculated (Table 1) from both FTIR (height method) and XRD (height method) according to the method and formulae used by the researchers [32,34–36]. It is briefly as follows; according to Reyes-Gasga et al. [32], for the FTIR (height method), heights of the bands at 603 (A_{603}), 569 (A_{569}) and 595 (A_{595}) cm^{-1} (lowest point between 603 and 569 cm^{-1}) are measured by forming baseline and value of crystallinity index $(CI)_{FTIR}$ is calculated through the following relation;

$$(CI)_{FTIR} = \frac{A_{569} + A_{603}}{A_{595}}$$

For $(CI)_{XRD}$, heights of the reflections such as (202), (300), (211) and (112) are measured by forming baseline and $(CI)_{XRD}$ value is calculated by the given formula [32];

$$(CI)_{XRD} = \frac{a(112) + b(300) + c(202)}{h(211)}$$

It is clear that the (CI)XRD values cannot be directly compared with those of (CI)FTIR. The XRD method uses an average volume while the FTIR method uses average heights. Both methods should be considered qualitatively complementary and not quantitatively the same [32]. It is known that the high and low CI values are connected with more ordered and poorly crystallized crystals [34].

In FTIR, the double sharp symmetrical bending strong peaks at 603/600 and 569/572 cm^{-1} (v_4) and in the case of XRD, reflections such as (202), (300), (211) and (112) located between 30° and 35° of the 2θ angle are taken for calculations. From Table 1, both CI values are high for NHAp, values are decreased for NHAp/PEG and low for NHAp/PVP. This dictates that degree of crystallinity is high for NHAp, it is decreasing while adding polymers, especially for NHAp/PVP has low degree of crystallinity as discussed elsewhere

(presence of triplet in FTIR, broadness of XRD peaks and result of SAED pattern). High substitution of CO_3^{2-} in NHAp/PVP reduces its crystallinity considerably [37]. NHAp with reduced crystallinity has high solubility and protein absorption capacity [33].

The present CI values are compared with different samples such as HAp prepared by precipitation method ((CI)FTIR = 3.67 to 6.07; (CI)XRD = 0 to 1.18) [32], fresh bone ((CI) FTIR = 2.8) [32], marine apatites ((CI) FTIR = 3.0 to 3.6) [35], HAp with different temperatures ((CI)FTIR = 4.63 to 7.80) [33] and modern bones ((CI)FTIR = 2.69 to 3.37) [34]. The present (CI)FTIR values are matched with CI values of fresh bone, while present (CI)XRD values are higher than HAp prepared by precipitation method [32].

3.2.2. Carbonate to phosphate (C/P) ratio

Carbonate to phosphate (C/P) ratio (Table 1) indicates the extent of carbonate incorporation (amount of carbonate) into the hydroxyapatite lattice. For the calculation, intensity of vibrational peak at 1443 cm^{-1} (amount of carbonate) is divided by the peak at 1048/1052 cm^{-1} (amount of phosphate) [34,38–42]. C/P value is low for NHAp (0.395), value is increases for NHAp/PEG (0.411) and high for NHAp/PVP (0.456). This dictates that the amount of carbonate content is high in NHAp/PVP, decreased in NHAp/PEG and low in NHAp as already discussed. The present ratio is compared with different samples such as CHAp prepared by chemical precipitation technique (0.185–0.231) [7], modern bone (0.31–0.65) [34] and fresh bone (~0.23) [40]. The present C/P values are comparable with modern bone and higher than other samples.

3.3. XRD analysis

Figure 2 demonstrates the X-ray diffraction patterns of NHAp (a), NHAp/PEG (b) and NHAp/PVP (c). In Figure 2 (a), identified reflections such as (111), (002), (210), (211), (112), (300), (202), (310), (222), (123) and (004) indicate the formation of hexagonal hydroxyapatite crystalline phase (JCPDS#09-0432) [3] in NHAp. The characteristic diffraction peaks are broadened, resolved and intensity decreases while adding the polymers when compared with Figure 2(a). These are high for NHAp/PVP. This dictates that the ratio between hexagonal lattice and primitive lattice is changed [15], crystallite size and crystalline nature are decreased when adding the polymers. The (210) peak is related to carbonate content, the intensity of the peak is increased when adding the polymers, especially, the intensity is so high in NHAp/PVP, these indicate the presence of B-type content in NHAp/PEG and NHAp/PVP [43–46]. According to Landi et al. [47], the presence of B-carbonate in the apatite lattice may decrease in crystallinity, increase in solubility in both in vitro and in vivo tests and higher affinity for the
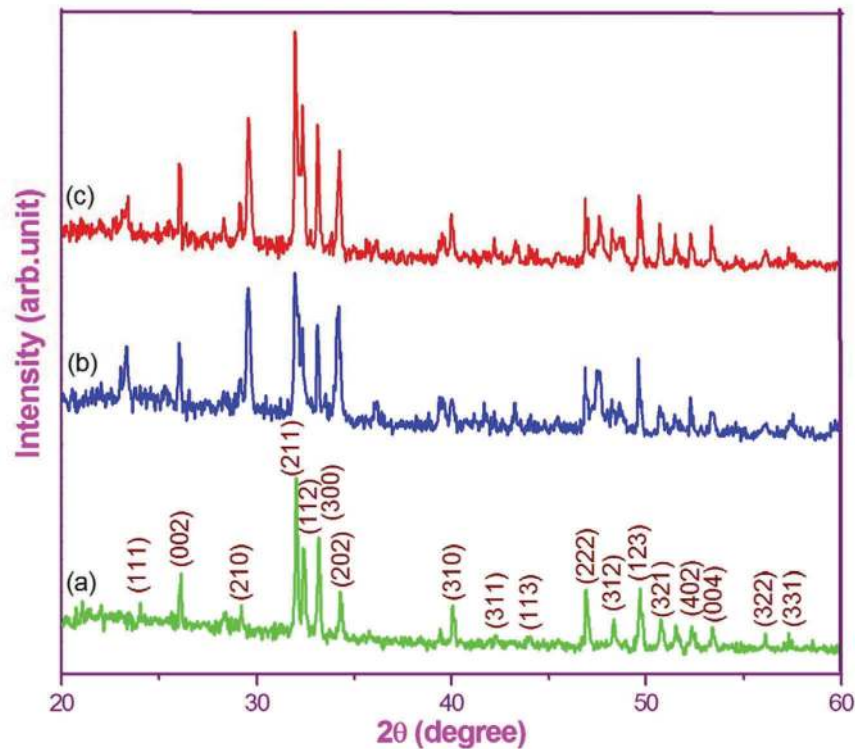
Figure 2. XRD patterns of the NHAp (a), NHAp/PEG (b) and NHAp/PVP (c) calcined at 900°C.

human trabecular osteoblastic cell. Whenever carbonate content is more, it mostly occupies the B sites [48]. Increased solubility in polymer composites may be due to the formation of $Ca_2HPO_4CO_3$ and $Ca_2PO_4CO_3$ [49]. HAp particles exhibit much higher tendency to grow along c-axis leads to increase the possibility of nanorods formations than particles [50]. This could be confirmed by the presence of (002) face. In the present case, the intensity of (002) is visible and high for NHAp/PVP.

3.3.1. Calculation of structural parameters

Crystallographic structural parameters of the NHAp are important because CO_3^{2-} substitution affects their physical parameters including lattice constants, crystallite size, crystalline nature, microstrain, dislocation density and stacking fault [37]. Since the stability, chemical reactivity, opacity, efficacy of delivery, flowability, texture, packing density, viscosity, porosity and strength of materials are affected by the above mentioned physical parameters [18], it is essential to calculate for the present samples (Table 1) based on the literature [32,51]. Dislocation density (δ) and stacking fault (SF) of the products are increased; plastic deformation and hardness of the products are also increased [51].

Calculated lattice constants are well matched with the above mentioned JCPDS (Table 1). When adding the polymers, values of lattice constant "a" and "c" are decreased and increased, respectively. For NHAp/PVP, low "a" and high "c" values are observed (Table 1). These indicate that "a" axis is contracted and "c" axis

expanded when carbonate content is more [52], and the c-lattice parameters increase could be due to the slight lengthening of T–O_3. Thus, the vacancies created at some of the O_3 sites effect in an enlargement of the channel radius, thereby increasing of solubility of the material [37]. These changes in the lattice constants and c/a ratio increased from 0.720 (NHAp) to 0.734 (NHAp/PVP) (Table 1) also indicate the presence of type B carbonate in NHAp [2,47].

The average crystallite sizes of NHAp, NHAp/PEG and NHAp/PVP are also calculated (Table 1) using well-known Debye-Scherrer formula [51]. From Table 1, the calculated crystallite size is lowered for NHAp/PEG and NHAp/PVP. Amongst, NHAp/PVP shows low crystallite size. Here in both cases, nucleation rate dominates the growth rate that decreases the crystallite size. PEG and PVP polymer with more functional groups cover large surface area of the nanoparticles with higher additional steric hindrance causing on negative effect on the growth of the crystal particle [15].

Especially, PVP is the surface-regulating polymer to regulate the nucleation and growth of NHAp. PVP stabilizes the nanoparticles through higher additional steric hindrance [15]. When PVP coated in NHAp, due to its severe physical action on the particles, high growth-blocking action occurs [18]. Even though both PEG and PVP are nonionic surfactants, they are charged partially. However, due to the more polar activity in PVP than PEG, it is more strongly adhere to the surface of NHAp [30].

While adding the polymers, values of all the structural parameters (ε, δ and SF) are increased (Table 1), especially NHAp/PVP shows high values. Thus, NHAp/PVP exhibits good plastic deformation and hardness. Grain size decreases with increasing strain lead to increases in the dislocation density and strength of materials. The same observations were achieved in the following literature [53]. The increases in structural parameters (ε, δ and SF) confirm the decrease in the crystalline nature (Table 1). According to de Carvalho Almança Lopes et al. [2], the presence of CO_3^{2-} in the HAp structure could be highly important because it could be the main source of distortion of the crystalline network, creating micro-stresses and defects in its vicinity, greatly influencing its solubility. This is achieved in the present study and hence NHAp/PVP has favorable mechanical property and solubility for biomedical applications.

3.4. Surface Morphology – SEM

SEM images of NHAp, NHAp/PEG and NHAp/PVP (Figure 3(a,c,d)) show flake, aggregated hexagonal particles and rod-like structures, respectively. Some of them are bonded together as aggregates (mostly hexagonal like) when adding PEG. The smaller size of the grains and aggregates could provide a higher specific surface area [54]. Generally, coordination bonds or strong interactions of the functional head groups of the polymers have the strong ability to interact with nanoparticles and thus kinetically control the growth rates of various faces of crystals, which could control the morphology. The structure of the PEG consists of hydrophilic – O – and hydrophobic – CH2–CH2 – in the long chain. The oxygen atom in PEG has coordination abilities and negative charge which can bind more strongly with positively charged NHAp ions due to the electrostatic forces of attraction [55]. Thus, PEG acted as an inhibitor and confined the hexagonal morphology based on the degree of adsorption, the electrostatic force of attraction and interaction between the PEG molecules and Ca^{2+} ionic group [56].

When adding PVP on NHAp, the nanoparticles are formed as clusters of nanorods with defined boundaries (Figure 3(d)). PVP greatly facilitates the formation of NHAP nanorods which is already assessed by c-axis increase and presence of (002) peak in XRD. For the formation of nanorod, large driving force could be acted to maximize the contact area and minimize the surface energy. PVP restricts growth along the side faces and activates growth along the end direction (c-axis), resulting in NHAp nanorods [57]. Many literature show that HAp prepared by precipitation method could be rod-like nanostructures preferably.

As in the case of biomineralization process, here also the similar effect could be happened for getting the rod like morphology. Two effects such as (i) spatial effect and (ii) electrostatic and hydrogen bond effects are important roles of PVP. The N–C = O group in PVP maybe preferentially adsorbed on the faces parallel to
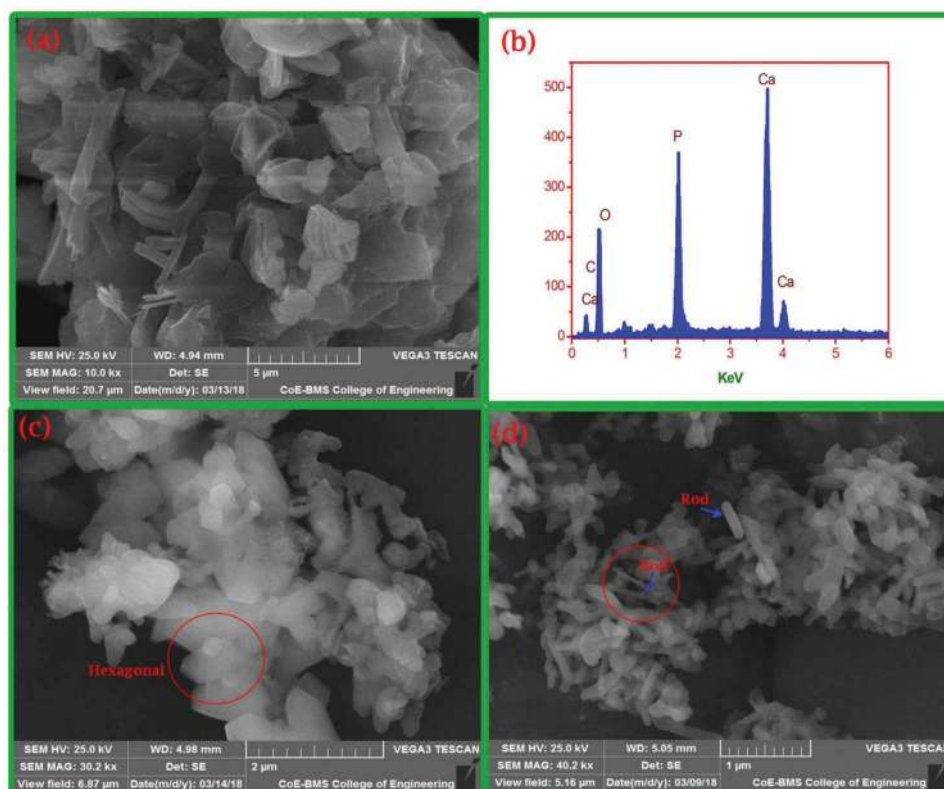

Figure 3. SEM images of NHAp (a), NHAp/PEG (c) and NHAp/PVP (d); EDX spectra of NHAp (b).

the (001) axis direction of NHAp as PVP has a polyvinyl skeleton with polar group, leads to preferential growth along the (001) direction, which support the directional growth of nanorods. The hydrogen bond is formed between PVP and NHAp through the abundant O–H groups located on the surface of NHAp, which restricts the nanorods aggregation and the growth of vertical to the c-axis direction [58].

In the present case, the formation of rod-like NHAp includes nucleation, surface-regulation, growth, oriented attachment and Ostwald ripening. Small-sized NHAp could be grown to the large rod-like NHAp due to the oriented attachment and Ostwald ripening process. By the strong effect of Vander Waals attraction, rod-like NHAp could aggregate together and form rod-like structure [58]. This is the possible mechanism for NHAp nanorod. The mechanism for the formation of HAp nanorod while adding PVP is clearly explained in the literature [18,57–59]. The present study also strongly believed that the above mentioned same mechanism could be involved in the present NHAp. These rod-like shapes are highly preferred morphology in various applications which include constructing the microstructure of teeth [50,60], bone tissue engineering [61,62], drug delivery systems [63] and other biomedical applications [61,63].

Figure 3(b) represents the EDX spectra of the NHAp. From the result, the presence of elements such as Ca, P, C and O is observed and the calculated Ca/P ratio is 1.68 which is well in accordance with theoretical ratio. For NHAp/PEG and NHAp/PVP, the ratios are 1.69 and 1.73, respectively. Deviation in the NHAp/PVP from the theoretical ratio also indicates the high presence of carbonate in the lattice. The presence of carbonate is also assessed by CHNS analyzer. The results show that percentage of carbonate in NHAp, NHAp/PEG and NHAp/PVP is 1.82%, 4.23% and 6.24% respectively.

3.5. TEM analysis

TEM images of NHAp, NHAp/PEG and NHAp/PVP are shown in Figure 4(a–c) respectively. Figure 4(a) shows NHAp morphology which indicates the particles with slight agglomeration. The hexagonal shape with slight agglomeration is observed when PEG is added in NHAp (NHAp/PEG) (Figure 4(b)). The formation of rod shape is visualized while adding PVP in the NHAp crystal structure during the synthesis process, which can have an effect on the nucleation of particles and can confine to particle agglomeration. The sizes of the nanorods are around diameter 76–134 nm and length 210–476 nm. These observations are well matched with the surface morphology of SEM analysis (Figure 3(a,c,d)).

The selected area electron diffraction (SAED) results of NHAp, NHAp/PEG and NHAp/PVP are shown in

Figure 4(d–f), respectively. The orderly spots confirm that the NHAp has crystalline nature (Figure 4(d)), when adding of polymer (PEG), the crystalline nature is slightly decreasing (Figure 4(e)). Figure 4(f) shows the further decrease in crystalline nature in NHAp/PVP as already discussed.

3.6. Antibacterial activity

The antibacterial activities of the sintered NHAp, NHAp/PEG and NHAp/PVP calcined at 900ºC were assessed against the E. coli and S. aureus (Figure 5), and the zone of inhibition of the samples is shown in Figure 6. The zone of inhibition increases when adding the polymers and it is high for NHAp/PVP (Figure 6). From the above result, it is found that the NHAp/PVP has good sensible antibacterial activity against the bacteria strains. According to Jadalannagari et al. [64], HAp with low crystalline nature has better rate of dissolution and better antibacterial activity as indicated by the larger zone of inhibition. It is matched with the present study. The electrostatic interaction between positively charged divalent ions and negatively charged ions from polymers could enhance the bactericidal effect. Negative ions may attract the ions causing stability (Ca^{2+}) to the cell wall of bacteria and are replaced by H^+ ions. Due to the high negativity in PVP, more ion exchange can be possible in NHAp/PVP. This may lead to cell membrane integrity loss, DNA rupture and cell death which appeared as inhibition zone [65]. Recently, Metha and Kaith [64] reported about the sensible antibacterial property of HAp against the same bacterial strains and got comparable zone of inhibition values.

It is interesting to note that NHAp/PVP exhibits less crystalline nature, low crystallite size, high carbonate content, suitable mechanical property, rod-like morphology and high antibacterial effect which are mainly necessary for biomedical applications, especially for bone-related applications. Thus, the NHAp/PVP is taken for further applications.

3.7. Hemolytic assay

Hemocompatibility is an important parameter of the materials which are used as implants or in direct contact with blood [65]. It was checked for NHAp/PVP (500 μg/mL) by hemolytic study [20] and the hemolytic ratio is 1.04 which is <2. As per ASTM 756–00 standard, samples with H value < 2 can be classified as non-hemolytic. Thus, NHAp/PVP is classified as non-hemolytic and exceedingly hemocompatible in nature with human blood. Crystalline behavior of NHAp/PVP favors for the non-hemolytic nature [64]. Photograph of hemolytic results is shown in Figure 7.
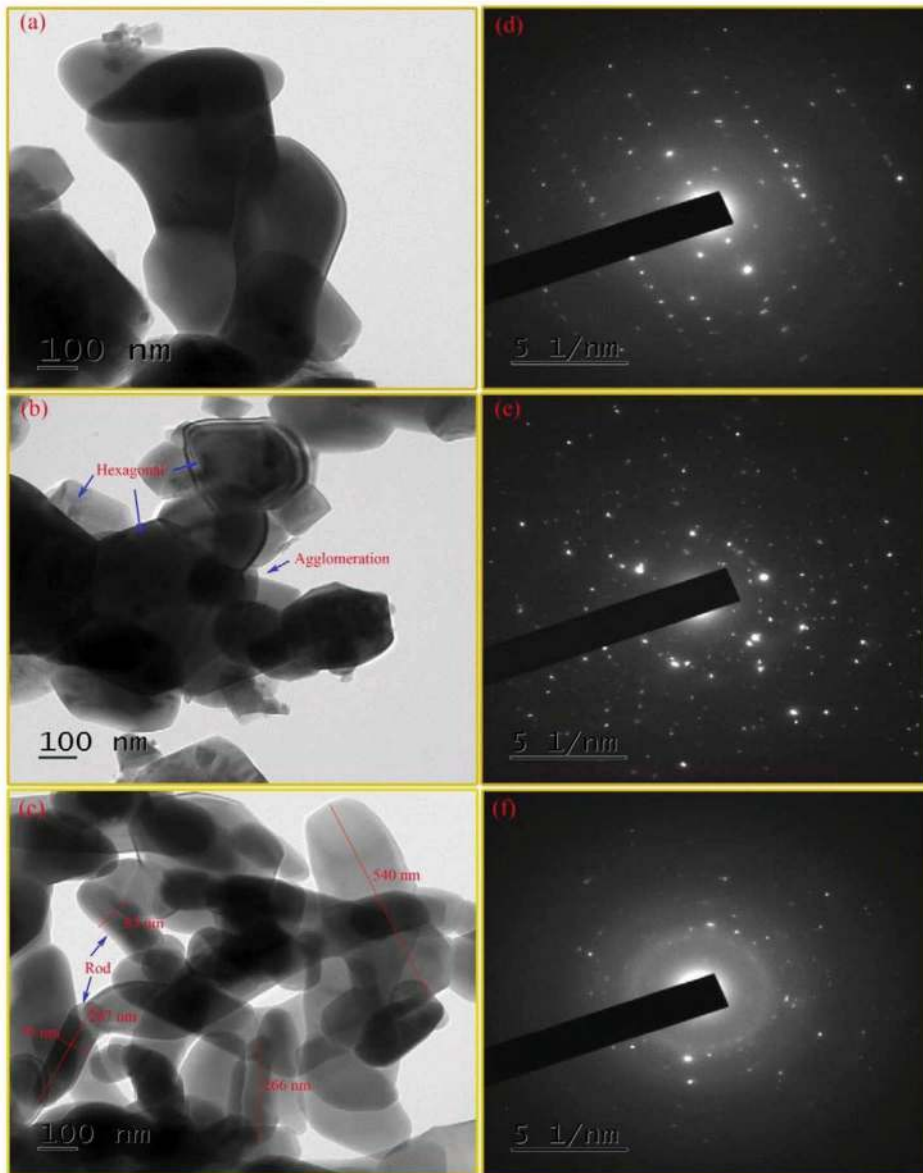
Figure 4. TEM images of NHAp (a), NHAp/PEG (b), NHAp/PVP (c) and SAED Patterns of NHAp (d), NHAp/PEG (e) and NHAp/PVP (f).
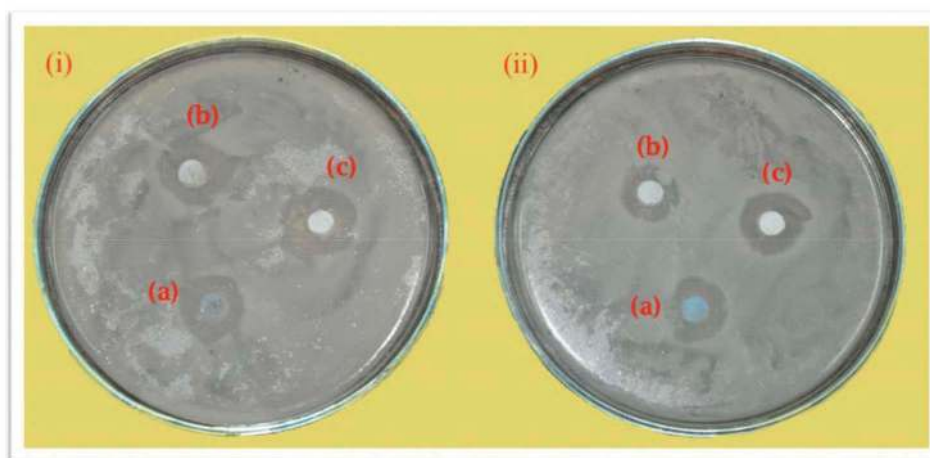

Figure 5. The antibacterial activity of the samples against *E. coli* (i) and *S. aureus* (ii). Note: (a), (b) and (c) respectively, represent NHAp, NHAp/PEG and NHAp/PVP.
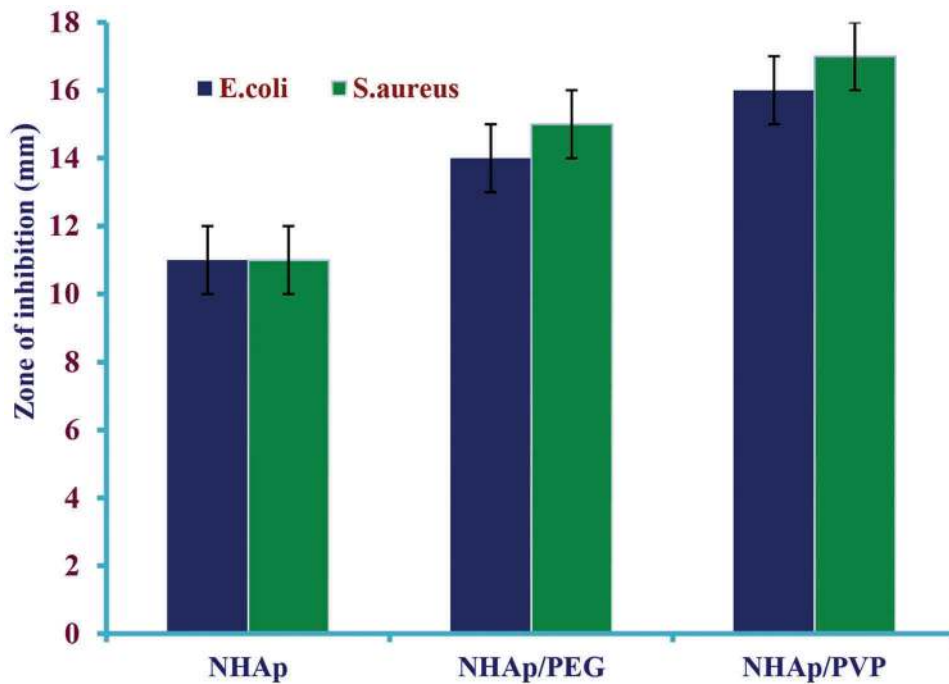
Figure 6. Zone of inhibition of the NHAp, NHAp/PEG and NHAp/PVP against *E. coli* and *S. aureus* with error bar.

3.8. SBF analysis – morphological observation

The present study intended to examine the apatite forming ability of NHAp/PVP nanoparticles for various days (3, 7 and 14 days) at 37 ± 0.5°C. Figure 8(a–c) shows the surface morphology of the NHAp/PVP nanoparticles after being soaked in SBF for 3, 7 and 14 days, respectively. The surface of all the NHAp/PVP (3, 7 and 14 days) nanoparticles shows the apatite formation, but the amount of apatite formed and the surface coverage varied specifically. At 3 days after immersion in SBF solution (Figure 8(a)), the surface is not completely covered with apatite growth. Figure 8(b) shows irregular apatite growth of NHAp/PVP at 7 days after immersion in SBF solution. At 15 days after immersion in SBF solution (Figure 8(c)), the surface of NHAp/PVP is completely covered by more apatite growth. The presence of pores and the formation of a dense apatite layer are observed on NHAp/PVP nanoparticles. These apatite structures on the sample can improve the osteoconduction and osteointegration properties [66]. Hence, apatite forming ability is favorable for NHAp/PVP nanoparticles at 14 days of immersion in SBF solution, whereas for 3 and 7 days of immersion, apatite growth is poor and incomplete.

The calcium and phosphate ions from the SBF could be consumed to grow the apatite on the surface of
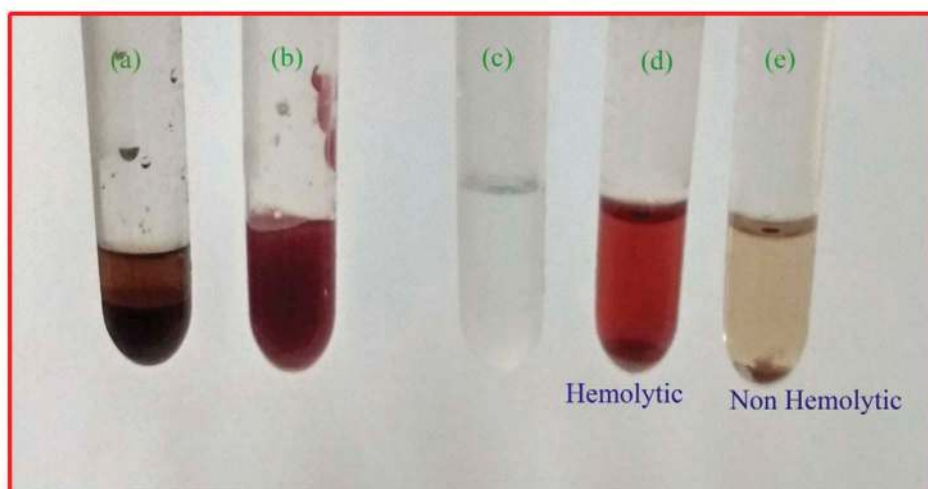

Figure 7. Photographic images of hemolysis assay: RBCs and blood plasma (a), RBCs (b), PBS (c), RBCs with PBS (d) and RBCs with sample NHAp/PVP (e).
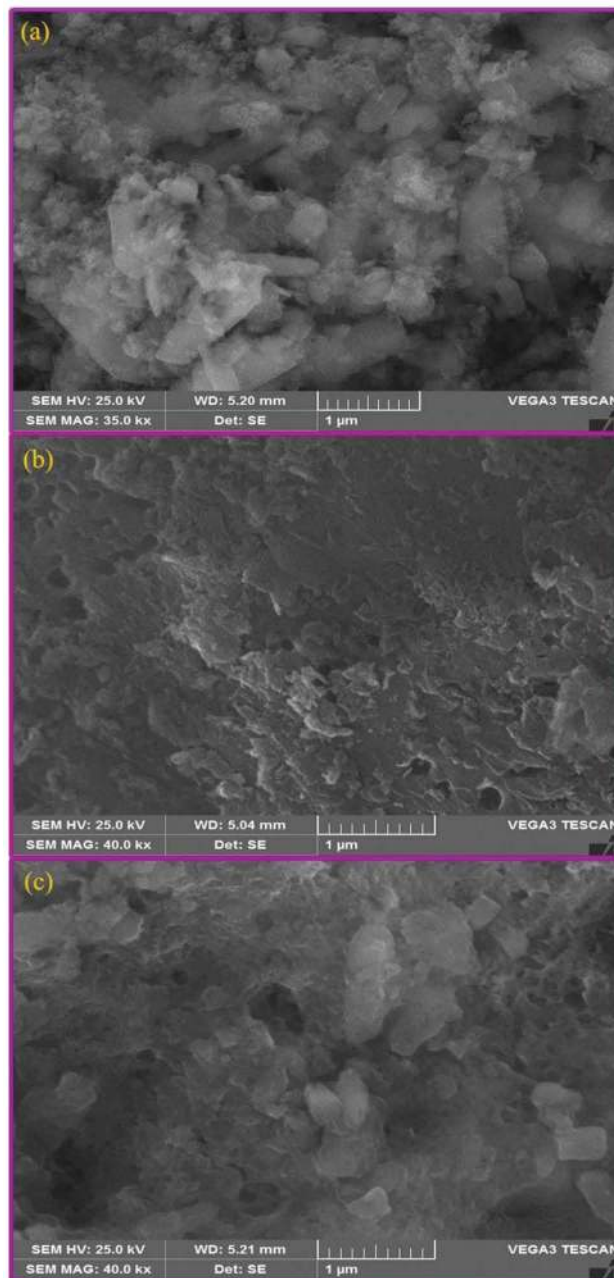
Figure 8. Surface morphology of the NHAp/PVP nanorods soaked in SBF for 3 (a), 7 (b) and 14 (c) days.

NHAp/PVP. It has been suggested that surface chemistry plays an important role in this process even the functional groups of materials have a large effect on the bone bonding property [67]. Negative groups (OH^- and PO_4^{3-}) are important for the apatite formation [68]. During soaking period, the positive ions include Ca^{2+}, Mg^{2+} and Na^{2+} from SBF are attracted by the surface PO_4^{3-} ions presented in the sample. The ion exchange between NHAp/PVP and SBF solution is influenced to form the apatite crystal. More CO_3^{2-} presence in the NHAp/PVP is also favorable for apatite formation. At the end of the precipitation, formed big salt chunks were properly washed and thus the surface gains positive charge and attracts the negatively charged OH^- and PO_4^{3-} ions from the SBF. This leads to the formation of the apatite layer on mineralized bioceramic nanomaterial.

4. Conclusion

NHAp, NHAp/PEG and NHAp/PVP have been successfully prepared by the chemical precipitation method from *clam shell* and are characterized. Formations of NHAp in the products are assessed by the presence of functional groups and characteristic planes of XRD. More carbonate presence in NHAp/PVP reveals the reduction of crystallite size and crystalline nature, increases in the c-axis, decreases in the a-axis, favorable mechanical property, deviation in the Ca/P ratio, high zone of inhibition, non-hemolytic activity and

good SBF interaction. The above mentioned properties are required for bone-related applications and forming apatite. Both SEM and TEM analyses show the same morphology. From the proposed mechanism, higher additional steric hindrance could play for reduction of crystallite size due to the growth blocking action, and for hexagonal morphology, oxygen atom in PEG could role by electrostatic forces of attraction between the negatively charged ions and positively charged NHAp ions. NHAp/PVP nanorods fashioned through the hydrogen bond formed between PVP and NHAp through the abundant O–H groups located on the surface of NHAp, and also Ostwald ripening and Oriented attachment could strongly play for nanorods growth. Crystalline nature and amount of carbonate content of the products are assessed through different ways and they are positively correlated with each other. The antibacterial activities of synthesized products demonstrated that high antibacterial activity is observed in NHAp/PVP due to the high negativity in PVP and low crystallite size. Good results are achieved in all analyses for NHAp/PVP. It is exceedingly hemo-compatible in nature with human blood due to the poor crystalline behavior. Finally, NHAp/PVP is applied in SBF analysis at three different times, apatite forming ability is favorable at 14 days of immersion due to the ion exchange between NHAp/PVP and SBF solution, here also, presence of more CO_3^{2-} is favorable for apatite formation. Thus, as obtained properties of the NHAp/PVP derived from *clam shell* are similar to those of the hydroxyapatite mineral existing in the human bones, it has prospective for bone-related applications.

Acknowledgments

Disclosure statement

No potential conflict of interest was reported by the authors.

Funding

ORCID

C. Suresh Kumar 🆔 http://orcid.org/0000-0003-1104-1070
K. Dhanaraj 🆔 http://orcid.org/0000-0001-5504-3604
R.M. Vimalathithan 🆔 http://orcid.org/0000-0002-3310-7985
P. Ilaiyaraja 🆔 http://orcid.org/0000-0002-9549-4837
G. Suresh 🆔 http://orcid.org/0000-0002-2525-1231

References

[1] Giraldo-Betancur AL, Epinosa-Arbelaez DG, Real-Lopez AD, et al. Comparison of physicochemical properties of bio and commercial hydroxyapatite. Curr Appl Phys. 2013;13(7):1383–1390.

[2] Lopes CD, Limirio PHJO, Novais VR, et al. Fourier transform infrared spectroscopy (FTIR) application chemical characterization of enamel, dentin and bone. Appl Spectrosc Rev. 2018;53(9):747–769.

[3] Riaz M, Zia R, Ijaz A, et al. Synthesis of monophasic Ag doped Hydroxyapatite and evaluation of antibacterial activity. Mater Sci Eng C. 2018;90:308–313.

[4] Othman R, Mustaf Z, Loon CW, et al. Effect of calcium precursors and pH on the precipitation of carbonated hydroxyapatite. Procedia Chem. 2016;19:539–545.

[5] Mishra VK, Bhattacharjee BN, Parkash O, et al. Mg-doped Hydroxyapatite nanoplates for biomedical applications: A surfactant assisted microwave synthesis and spectroscopic investigations. J Alloys Compd. 2014;614:283–288.

[6] Basu S, Basu B. Doped biphasic calcium phosphate: synthesis and structure. J Asian Ceram Soc. 2019;7 (3):265–283.

[7] Bang LT, Long BD, Othman R. Carbonate hydroxyapatite and silicon-substituted carbonate Hydroxyapatite: synthesis, mechanical properties, and solubility evaluations. Sci World J. 2014;2014:1–9.

[8] Wu SC, Tsou HK, Hsu HC, et al. A hydrothermal synthesis of eggshell and fruit waste extract to produce nano-sized hydroxyapatite. Ceram Int. 2013;39(7):8183–8188.

[9] Samant A, Nayak B, Misra PK. Kinetics and mechanistic interpretation of fluoride removal by nanocrystalline hydroxyapatite derived from Limacine artica shells. J Environ Chem Eng. 2017;5(6):5429–5438.

[10] Ancane KS, Stipniece L, Irbe Z. Effect of biogenic and synthetic starting materials on the structure of hydroxyapatite bioceramics. Ceram Int. 2016;42(8):9504–9510.

[11] Ramachandra TV, Boominathan M, Subash Chandran MD. Valuation of bivalves of Aghanashini estuary, Indian west coast. NeBIO. 2011;2(1).

[12] Bramhe S, Kim TN, Balakrishnan A, et al. Conversion from biowaste Venerupis clam shells to hydroxyapatite nanowires. Mater Lett. 2014;135:195–198.

[13] Vecchio KS, Zhang X, Massie JB, et al. Conversion of bulk seashells to biocompatible hydroxyapatite for bone implants. Acta Biomater. 2007;3(6):910–918.

[14] Yelten A, Yilmaz S. Various parameters affecting the synthesis of the hydroxyapatite powders by the wet chemical precipitation technique. Mater Today Proc. 2016;3(9):2869–2876.

[15] Qian G, Liu W, Zheng L, et al. Facile synthesis of three dimensional porous hydroxyapatite using carboxymethylcellulose as a template. Results Phys. 2017;7:1623–1627.

[16] Youness RA, Taha MA, Ibrahim MA. Effect of sintering temperatures on the in vitro bioactivity, molecular structure and mechanical properties of titanium/carbonated Hydroxyapatite nanobiocomposites. J Mol Struct. 2017;1150:188–195.

[17] Başargan T, Erdöl-Aydin N, Nasün-Saygili G. In situ biomimetic synthesis to produce HYDROXYAPATITE– POLYVINyl alcohol biocomposites: precipitation and

spray drying methods. Polym Plast Technol Eng. 2016;55(5):447–452.

[18] Barabas R, Czik M, Dekany I, et al. Comparative study of particle size analysis of Hydroxyapatite-based nanomaterials. Chem Pap. 2013;67(11):1414–1423.

[19] Dhanaraj K, Suresh G. Conversion of waste sea shell (Anadara granosa) into valuable nanohydroxyapatite (nHAp) for biomedical applications. Vacuum. 2018;152:222–230.

[20] Tank KP, Chudasama KS, Thaker VS, et al. Pure and zinc doped nano-hydroxyapatite: synthesis, characterization, antimicrobial and hemolytic studies. J Cryst Growth. 2014;401:474–479.

[21] Adler HH, Kerr PF. Infrared study of aragonite and calcite. Am Mineral. 1962;47:700–717.

[22] Tangboriboon N, Kunanuruksapong R, Sirivat A. Preparation and properties of calcium oxide from eggshells via calcinations. Mater Sci-Poland. 2012;30 (4):313–322.

[23] Youness RA, Taha MA, Elhaes H, et al. Molecular modeling, FTIR spectral characterization and mechanical properties of carbonated-Hydroxyapatite prepared by mechanochemical synthesis. Mater Chem Phys. 2017;190:209–218.

[24] Lala S, Ghosh M, Das PK, et al. Magnesium substitution in carbonated Hydroxyapatite: structural and microstructural characterization by Rietveld's refinement. Mater Chem Phys. 2016;170:319–329.

[25] Núñez D, Elgueta E, Varaprasad K, et al. Hydroxyapatite nanocrystals synthesized from calcium rich bio-wastes. Mater Lett. 2018;230:64–68.

[26] Chaudhry AA, Knowles JC, Rehman I, et al. Rapid hydrothermal flow synthesis and characterisation of carbonate- and silicate-substituted calcium phosphates. J Biomater Appl. 2013;28(3):448–461.

[27] Tkalcec E, Popovic J, Orlic S, et al. Hydrothermal synthesis and thermal evolution of carbonate-fluorhydroxyapatite scaffold from cuttlefish bones. Mater Sci Eng C. 2014;42:578–586.

[28] Rey C, Collins B, Goehl T, et al. The carbonate environment in bone mineral: A resolution-enhanced Fourier Transform Infrared Spectroscopy study. Calcif Tissue Int. 1989;45(3):157–164.

[29] Ren F, Ding Y, Leng Y. Infrared spectroscopic characterization of carbonated apatite: a combined experimental and computational study: IR spectroscopic characterization of CAp. J Biomed Mater Res A. 2014;102(2):496–505.

[30] Thirugnanam T. Effect of polymers (PEG and PVP) on sol-gel synthesis of microsized Zinc oxide. J Nanomater. 2013;2013:1–7.

[31] Pleshko N, Boskey A, Mendelsohn R. Novel infrared spectroscopic method for the determination of crystallinity of hydroxyapatite minerals. Biophys J. 1991;60 (4):786–793.

[32] Reyes-Gasga J, Martinez-Pineiro EL, Rodriguez-Alvarez G, et al. XRD and FTIR crystallinity indices in sound human tooth enamel and synthetic hydroxyapatite. Mater Sci Eng C. 2013;33:4568–4574.

[33] Sa Y, Guo Y, Feng X, et al. Are different crystallinity-index-calculating methods of hydroxyapatite efficient and consistent? New J Chem. 2017;41 (13):5723–5731.

[34] Nagy G, Lorand T, Patonai Z, et al. Analysis of pathological and non-pathological human skeletal remains by FT-IR spectroscopy. Forensic Sci Int. 2008;175 (1):55–60.

[35] Shemesh A. Crystallinity and diagenesis of sedimentary apatite. Geochim Cosmochim Acta. 1990;54 (9):2433–2438.

[36] Person A, Bocherens H, Saliege JF, et al. Early diagenetic evolution of bone phosphate: an X-ray diffractometry analysis. J Archaeol Sci. 1995;22(2):211–221.

[37] Leventouri TH, Chakoumakos BC, Papanearchou N, et al. Crystal structure studies of natural and synthetic apatite by neutron powder diffraction. Mater Sci Forum. 2001;378–381:517–522.

[38] Wright LE, Schwarcz HP. Infrared and isotopic evidence for diagenesis of bone apatite at Dos Pilas, Guatemala: palaeodietary implications. J Archaeol Sci. 1996;23(6):933–944.

[39] Koon HEC, Nicholson RA, Collins MJ. A practical approach to the identification of low temperature heated bone using TEM. J Archaeol Sci. 2003;30 (11):1393–1399.

[40] Olsen J, Heinemeier J, Bennike P, et al. Characterisation and blind testing of radiocarbon dating of cremated bone. J Archaeol Sci. 2008;35(3):791–800.

[41] Thompson TJU, Gauthier M, Islam M. The application of a new method of Fourier Transform Infrared Spectroscopy to the analysis of burned bone. J Archaeol Sci. 2009;36(3):910–914.

[42] Thompson TJU, Islama M, Piduru K, et al. An investigation into the internal and external variables acting on crystallinity index using Fourier Transform Infrared Spectroscopy on unaltered and burned bone. Palaeogeogr Palaeoclimatol Palaeoecol. 2011;299(1–2):168–174.

[43] Cahyaningrum SE, Herdyastuty N, Devina B, et al. Synthesis and characterization of hydroxyapatite powder by wet precipitation method. IOP Conf Ser Mater Sci Eng. 2017;299:012039.

[44] Tay FR, Pashley DH, Rueggeberg FA, et al. Calcium phosphate phase transformation produced by the interaction of the portland cement component of white mineral Trioxide aggregate with a phosphate-containing fluid. J Endod. 2007;33(11):1347–1351.

[45] Sakae T. Variations in dental enamel crystallites and micro-structure. J Oral Biosci. 2006;48(2):85–93.

[46] Raya I, Mayasari E, Yahya A, et al. Synthesis and characterizations of calcium hydroxyapatite derived from crabs shells (portunus pelagicus) and its potency in safeguard against to dental demineralizations. Int J Biomater. 2015;2015:4691768.

[47] Landi E, Celotti G, Logroscino G, et al. Carbonated Hydroxyapatite as bone substitute. J Eur Ceram Soc. 2003;23(15):2931–2937.

[48] Vignoles M, Bonel G, Holcomb DW, et al. Influence of preparation conditions on the composition of type b carbonated hydroxyapatite and on the localization of the carbonate ions. Calcif Tissue Int. 1988;43(1):33–40.

[49] Pan H, Darvell BW. Effect of carbonate on hydroxyapatite solubility. Cryst Growth Des. 2010;10(2):845–850.

[50] Klinkaewnarong J, Utara S. Ultrasonic-assisted conversion of limestone into needle-like hydroxyapatite nanoparticles. Ultrason Sonochem. 2018;46:18–25.

[51] Ramasamy V, Anand P, Suresh G. Synthesis and characterization of polymer-mediated $CaCO_3$ nanoparticles using limestone: A novel approach. Adv Powder Technol. 2018;29(3):818–834.

[52] Leventouri TH, Chakoumakos BC, Papanearchou N, et al. Comparison of crystal structure parameters of natural and synthetic apatites from neutron powder diffraction. J Mater Res. 2001;16(9):2600–2606.

[53] Ramasamy V, Vijayalakshmi G. Effect of Zn doping on structural optical and thermal properties of CeO_2 nanoparticles. Superlattice Microstruct. 2015;85:510–515.

[54] Viriya-empikul N, Krasae P, Nualpaeng W, et al. Biodiesel production over Ca-based solid catalysts derived from industrial wastes. Fuel. 2012;92(1):239–244.

[55] Shi X, Li M, Yang H, et al. PEG-300 assisted hydrothermal synthesis of $4ZnO.B_2O_3.H_2O$ nanorods. Mater Res Bull. 2007;42(9):1649–1656.

[56] Parra MR, Haque FZ. Poly (Ethylene Glycol) (PEG)-assisted shape-controlled synthesis of one-dimensional ZnO nanorods. Optik. 2015;126(18):1562–1566.

[57] Nathanael AJ, Seo YH, Oh TH. PVP assisted synthesis of hydroxyapatite nanorods with tunable aspect ratio and bioactivity. J Nanomater. 2015;2015:1–9.

[58] Zhang Y, Lu J. A mild and efficient biomimetic synthesis of rodlike hydroxyapatite particles with a high aspect ratio using polyvinylpyrrolidone as capping agent. Cryst Growth Des. 2008;8(7):2101–2107.

[59] Nathanael AJ, Han SS, Oh TH. Polymer-assisted hydrothermal synthesis of hierarchically arranged hydroxyapatite nanoceramic. J Nanomater. 2013;2013:962026.

[60] Sanosh KP, Chu MC, Balakrishnan A, et al. Synthesis of nano Hydroxyapatite powder that simulate teeth particle morphology and composition. Curr Appl Phys. 2009;9(6):1459–1462.

[61] Hasuwan PK, Kuanchertchoo N, Wetprasit N, et al. Hydroxyapatite/ovalbumin composite particles as model protein carriers for bone tissue engineering: I. Synthesis and characterization. Mater Sci Eng C. 2012;32(4):758–762.

[62] Bricha M, Belmamouni Y, Essassi EM, et al. Surfactant-assisted hydrothermal synthesis of hydroxyapatite nanopowders. J Nanosci Nanotechnol. 2012;12 (10):8042–8049.

[63] Leena M, Rana D, Webster TJ, et al. Accelerated synthesis of biomimetic nano hydroxyapatite using simulated body fluid. Mater Chem Phys. 2016;180:166–172.

[64] Jadalannagari S, Deshmukh K, Ramanan SR, et al. Antimicrobial activity of hemocompatible silver doped hydroxyapatite nanoparticles synthesized by modified sol–gel technique. Appl Nanosci. 2014;4 (2):133–141.

[65] Mehta P, Kaith BS. In-situ fabrication of rod shaped nano-hydroxyapatite using microwave assisted semi-interpenetrating network as a template-morphology controlled approach. Mater Chem Phy. 2018;208:49–60.

[66] Gopi D, Ramya S, Rajeswaria D, et al. Strontium, cerium co-substituted hydroxyapatite nanoparticles: synthesis, characterization, antibacterial activity towards prokaryotic strains and in vitro studies. Colloid Surf A. 2014;451:172–180.

[67] Gopi D, Nithiya S, Shinyjoy E, et al. Spectroscopic investigation on formation and growth of mineralized nanohydroxyapatite for bone tissue engineering applications. Spectrochim Acta Part A. 2012;92:194–200.

[68] Ananth KP, Shanmugam S, Jose SP, et al. Structural and chemical analysis of silica-doped –TCP ceramic coatings on surgical grade 316L SS for possible biomedical application. J Asian Ceram Soc. 2015;3:317–324.